Letter

Signature of topological band crossing in ferromagnetic $Cr_{1/3}NbSe_2$ epitaxial thin film

Bruno Kenichi Saika,[1] Satoshi Hamao,[1] Yuki Majima,[1] Xiang Huang,[1] Hideki Matsuoka,[2] Satoshi Yoshida,[1] Miho Kitamura,[3] Masato Sakano,[1,4] Tatsuto Hatanaka,[1] Takuya Nomoto,[5] Motoaki Hirayama,[1,2,4] Koji Horiba,[3] Hiroshi Kumigashira,[6] Ryotaro Arita,[5,2] Yoshihiro Iwasa,[1,2,4] Masaki Nakano,[1,2,4] and Kyoko Ishizaka[1,2,4]

[1]*Department of Applied Physics, University of Tokyo, Tokyo 113-8654, Japan*
[2]*RIKEN Center for Emergent Matter Science (CEMS), Wako 351-0198, Japan*
[3]*Photon Factory, Institute of Materials Structure Science, High Energy Accelerator Research Organization, Tsukuba 305-0801, Japan*
[4]*Quantum-Phase Electronics Center (QPEC), The University of Tokyo, Wako 113-8656, Japan*
[5]*Research Center for Advanced Science and Technology, University of Tokyo, Komaba Meguro-ku, Tokyo 153-8904, Japan*
[6]*Institute of Multidisciplinary Research for Advanced Materials (IMRAM), Tohoku University, Sendai 980-8577, Japan*

(Received 30 April 2022; accepted 3 October 2022; published 4 November 2022)

In intercalated transition metal dichalcogenides (I-TMDCs), transition metal intercalation introduces magnetic phases which in some cases induce topological band crossing. However, evidence of the topological properties remains elusive in such materials. Here, we employ angle-resolved photoemission spectroscopy to reveal the band structure of epitaxially grown ferromagnetic $Cr_{1/3}NbSe_2$. Experimental evidence of the Weyl crossing shows $Cr_{1/3}NbSe_2$ to be a topological ferromagnet. This Letter highlights I-TMDCs as a platform towards the interplay of magnetic and topological physics in low-dimensional systems.

DOI: 10.1103/PhysRevResearch.4.L042021

Nontrivial topology in the band structure of solids can have profound effects on the macroscopic properties of matter, with potential technological applications ranging from dissipationless transport to many exotic quasiparticle excitations [1–3]. Weyl semimetals refer to one of such topological phases, in which broken spatial-inversion or time-reversal symmetry gives rise to pairs of singularity points of source (positive chirality) or sink (negative chirality) of the Berry curvature [4–7]. To date, the majority of Weyl semimetals have been found in materials with broken inversion symmetry, such as TaAs [8,9], $PbTaSe_2$ [10,11], $TaIrTe_4$ [12,13], and $MoTe_2$ [14,15]. In addition, time-reversal symmetry breaking Weyl semimetals have also been found in ferromagnetic compounds such as Co_2MnGa [16,17] and $Co_3Sn_2S_2$ [18,19]. However, magnetic Weyl semimetals are still restricted to a small class of materials, and several predicted systems still lack experimental evidence. Expanding the family of time-reversal symmetry breaking Weyl systems is of extreme relevance, as varied magnetic textures are expected to couple with topologically nontrivial electronic structures to serve as a platform for emergent quantum phases. Additionally, novel routes towards accessing and controlling topological phases via external fields are expected in such coupled systems.

The 3*d* intercalated transition metal dichalcogenides (3*d* I-TMDCs) represent a class of intercalated layered materials which possess rich magnetic phases due to the localized magnetic moment of intercalants [20–22]. Recently, the magnetic 3*d* I-TMDCs have been reexamined under the framework of topological physics. The antiferromagnet $Co_{1/3}NbS_2$ has attracted considerable attention as potential noncollinear spin textures and topological band crossings were linked to the giant anomalous Hall effect observed in the compound [23–25]. Additionally, a first-principles calculation focused on the ferromagnetic 1/3-intercalated $M_{1/3}TX_2$ (M: 3*d* transition metal; T: Nb, Ta; X: S, Se) has suggested the presence of band crossing points in the electronic structure, indicating such systems to be candidates for magnetic Weyl materials [26]. However, several difficulties hinder the progress in these materials such as the lack of easy cleavage planes, and a surface disorder effect [27]. This stems from the nature of the intercalation itself, as the occupancy of intercalant atoms at the cleaved surface produces uncertain terminations. In addition, the study of the topological phases in I-TMDCs is complicated by complex magnetic ordering which provides a nontrivial modification to the electronic structure. Hence, a clear demonstration of such topologically nontrivial ferromagnetic phases requires 1/3-intercalated systems with accessible magnetic phases. From the consolidated ferromagnetic $M_{1/3}TX_2$ candidates, $Cr_{1/3}NbS_2$ and $Mn_{1/3}NbS_2$ exhibit complicated helimagnetic ordering, whereas the selenide counterpart $Cr_{1/3}NbSe_2$ exhibits a rather simpler easy-plane ferromagnetic phase [28,29]. Consequently, $Cr_{1/3}NbSe_2$ provides a suitable candidate for visualizing the predicted topological phases in 3*d* I-TMDCs.

In this Letter, motivated by the prospects of magnetic topological phases in 3*d* I-TMDCs, we provide evidence of the topologically nontrivial band structure of ferromagnetic $M_{1/3}TX_2$ by targeting $Cr_{1/3}NbSe_2$. We report the elec-

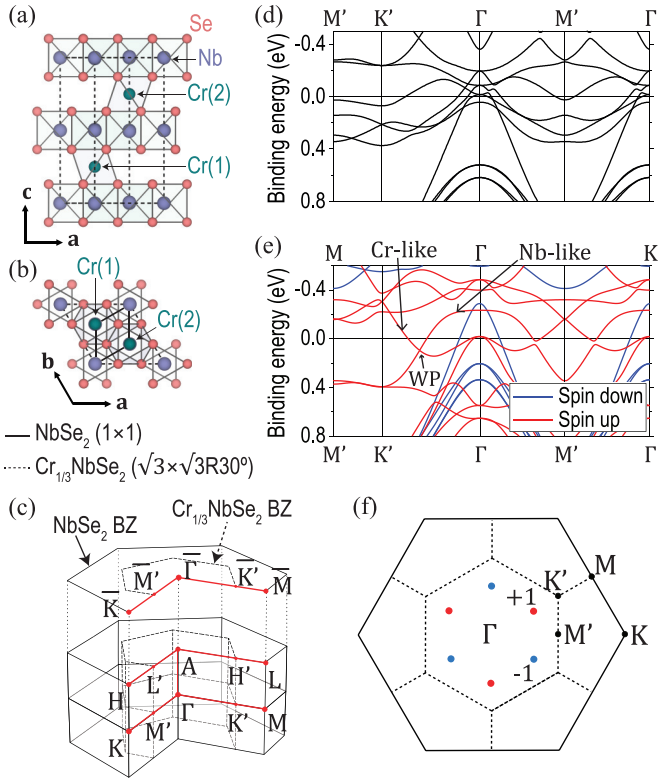

FIG. 1. Crystal structure and band calculation of $Cr_{1/3}NbSe_2$. Crystal structure viewed along the (a) *b* axis and (b) *c* axis. Solid and dotted lines denote the $NbSe_2(1 \times 1)$ and $Cr_{1/3}NbSe_2(\sqrt{3} \times \sqrt{3})R30^\circ$ cell, respectively. (b) Position of Cr(1) and Cr(2) atoms highlighted over the top view of $Cr_{1/3}NbSe_2$. (c) Hexagonal BZ and high-symmetry points of $NbSe_2$ (solid lines) and $Cr_{1/3}NbSe_2$ (dotted lines). Bulk band structure calculation in the (d) paramagnetic and (e) ferromagnetic states. Nb-like and Cr-like band crossing can be observed along Γ-*M* in the ferromagnetic band structure. (f) Schematic position of the WP. Red and blue colors denote the positive and negative chirality WP, respectively.

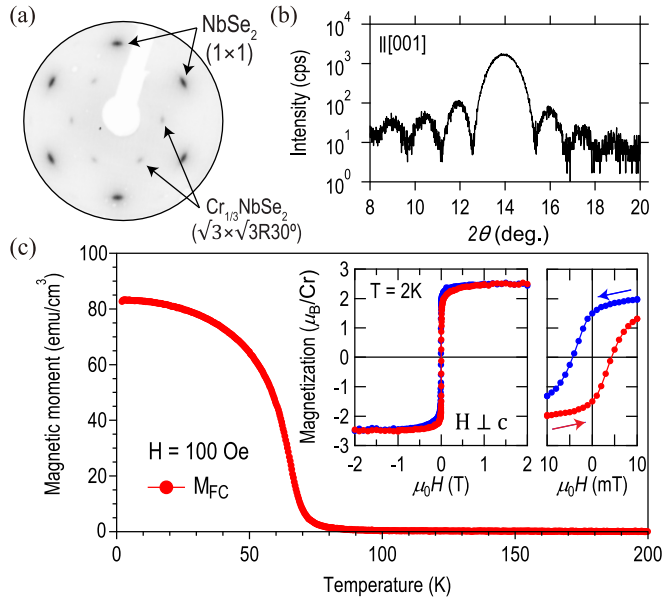

FIG. 2. $Cr_{1/3}NbSe_2$ thin-film characterization. (a) LEED pattern of $Cr_{1/3}NbSe_2$ taken at room temperature showing the presence of $(\sqrt{3} \times \sqrt{3})R30^\circ$ diffraction spots. (b) Out-of-plane XRD pattern exhibiting a Laue oscillation period. (c) Temperature dependence of the magnetic moment of the $Cr_{1/3}NbSe_2$ thin film. A magnetic field of 100 Oe was set parallel along the $NbSe_2$ layers ($H \perp c$). Inset left: In-plane magnetic field ($H \perp c$) dependence of the magnetization taken at 2 K (blue and red markers indicate the direction of the decreasing and increasing field sweep, respectively). Inset right: Closeup of the near zero-field magnetization.

tronic structure of $Cr_{1/3}NbSe_2$ fabricated via molecular beam epitaxy (MBE) and measured via angle-resolved photoemission spectroscopy (ARPES). We observe the correspondence between the electronic structure of the multilayer $Cr_{1/3}NbSe_2$ epitaxial thin films and the theoretical ferromagnetic bulk band structure. Through careful examination of the photoemission spectra, we find evidence of the Weyl crossing predicted in first-principles calculations.

The nine-layer $Cr_{1/3}NbSe_2$ thin films were fabricated onto atomically flat sapphire substrates using MBE, in which the number of layers is defined from the number of intercalant layers. Niobium was evaporated via an electron beam evaporator, whereas chromium and selenium were evaporated by standard Knudsen cells. The samples were grown and annealed at 850 °C under constant Se flux. A thick Se cap was deposited before exposure to the atmosphere for *ex situ* measurements. The growth procedure was monitored via reflection high-energy electron diffraction (RHEED). Prior to ARPES and low-energy electron diffraction (LEED) measurements, samples were annealed at temperatures above 170 °C in ultrahigh vacuum for cap removal. X-ray photoemission spectroscopy (XPS) and ARPES measurements were performed at 20 K in the photoelectron spectroscopy end station equipped with a Scienta-Omicron SES2002 electron analyzer at BL-2A (MUSASHI) in Photon Factory, Japan. Vacuum ultraviolet ARPES (VUV-ARPES) and soft x-ray ARPES (SX-ARPES) were conducted with photon energies ranging from 80 to 150 eV (circular polarization) and from 250 to 400 eV (linear polarization), respectively. The energy resolution was estimated to be 75 meV for VUV-ARPES, and 130 meV for SX-ARPES. The calculated band structure was obtained using the projector augmented wave (PAW) with the Perdew-Burke-Ernzerhof (PBE) exchange-correlation functional, as implemented in the Vienna *ab initio* simulation package (VASP) [30–33]. The cutoff energy and *k*-point mesh were set to 500 eV and 12 × 12 × 6, respectively.

The bulk crystal structure of $Cr_{1/3}NbSe_2$ is shown in Figs. 1(a) and 1(b). $NbSe_2$ layers are composed of Nb atoms surrounded by six Se atoms in trigonal prismatic coordination. The layers follow the $2H_a$ stacking order which creates octahedral sites at the van der Waals gaps directly above and below Nb atoms. As shown by the arrows in Figs. 1(a) and 1(b), Cr atoms occupy these 2*c* Wyckoff sites and construct a noncentrosymmetric structure described by the space group $P6_322$ [20,21,34,35]. Cr atom ordering creates a $(\sqrt{3} \times \sqrt{3})R30^\circ$ superstructure unit cell relative to the parent $NbSe_2$, which translates into a smaller hexagonal Brillouin zone (BZ) rotated 30° relative to the parent $NbSe_2$ BZ as shown in Fig. 1(c). To differentiate from the parent BZ, the

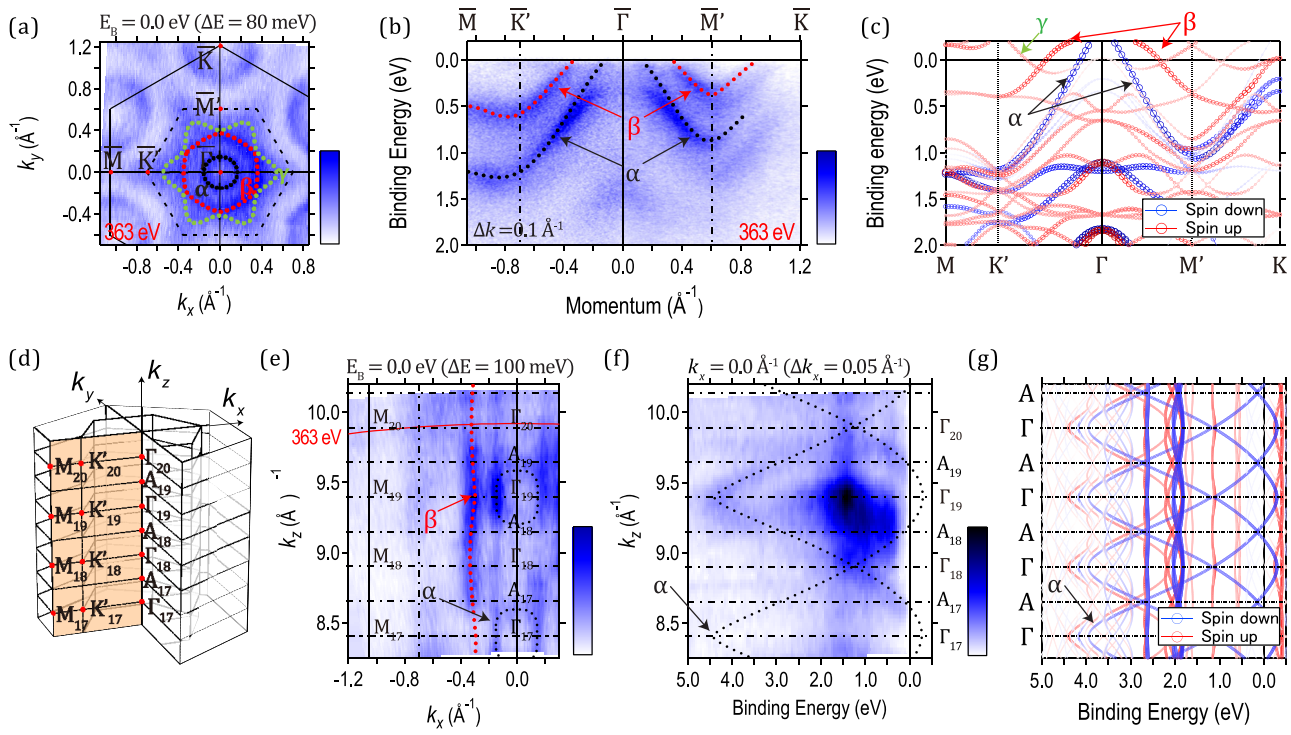

FIG. 3. SX-ARPES characterization of electronic structure. (a) FS mapping taken with 363 eV excitation energy and an integral window of 80 meV. Guide-for-the-eyes trace bands around $\overline{\Gamma}$ with labels α (black), β (red), and γ (green), respectively. (b) Dispersion taken with momentum windows of 0.1 Å^{-1} along the 2D high-symmetry points $\overline{M}$-$\overline{\Gamma}$-$\overline{K}$. (c) Band unfolding onto the original $NbSe_2$ BZ in the ferromagnetic state with blue (red) markers representing spin-down (up) bands. Arrows show corresponding α, β, and γ bands. (d) Schematic diagram of the measurement range along k_z. (e) Constant-energy mapping ($E_B = 0$ eV and integral window $\Delta E_B = 100$ meV) taken along k_z. The solid red line shows the cut corresponding to the 363 eV measurement shown in (a) and (b). Guide-for-the-eyes trace highlights the α and β bands along k_z. (f) Band dispersion along Γ-A (integral window $\Delta k_x = 0.1$ Å^{-1}). Guide-for-the-eyes trace the visible α bands. (g) Band-unfolding calculation along Γ-A.

high-symmetry points of the $Cr_{1/3}NbSe_2$ BZ are denoted with the prime symbol (M', K', H', and L'). Figures 1(d) and 1(e) show the calculated bulk band structures along M-Γ-K in the paramagnetic and ferromagnetic phases, respectively. As can be seen, the electronic bands near the Fermi level are strongly modified by introducing the magnetism. Notably, a band crossing close to the Fermi level is observed to occur along the Γ-M (Γ-K') direction in the ferromagnetic phase, originating from the spin-up components. According to calculation, this band crossing forms a Weyl point (WP), and the bands participating in the Weyl crossing correspond to the niobiumlike 4d and the chromiumlike 3d derived states. The Weyl points and the corresponding chirality are shown schematically relative to the original $NbSe_2$ BZ in Fig. 1(f). We also compared the calculated ferromagnetic band structure in the presence of spin-orbit coupling (SOC), in which the overall electronic structure is not significantly altered and the band crossing is still observed [36].

The characterization of $Cr_{1/3}NbSe_2$ epitaxial thin films is described in Fig. 2. The superstructure produced by Cr intercalation was confirmed via low-energy electron diffraction (LEED) in Fig. 2(a). The $(\sqrt{3} \times \sqrt{3})R30^\circ$ diffraction spots are clearly observed in the interior of the parent $NbSe_2$ diffraction pattern, indicating the 1/3-intercalation ratio of Cr atoms. The out-of-plane x-ray diffraction (XRD) taken along the [001] direction is shown in Fig. 2(b). The presence of a strong diffraction peak at $2\theta = 14^\circ$ along with Laue oscillation indicate the high crystalline quality of the film along the out-of-plane direction. The reported number of layers was obtained from the Laue oscillation period. We also performed x-ray photoemission spectroscopy (XPS) and observed the clear presence of Nb, Se, and Cr core-level spectra [36]. The magnetization as a function of temperature (M-T) measured in the field-cooling (FC) condition is displayed in Fig. 2(c), in which a magnetic field of 100 Oe was applied along the in-plane direction ($H \perp c$). The M-T curve clearly shows the presence of a magnetic phase transition at around 66 K, as defined from the maximum of the M-T curve derivative relative to temperature. The magnetic field dependence of the magnetization measured at 2 K is displayed in the inset of Fig. 2(c). The near zero-field magnetization is also shown in the right inset, in which a finite spontaneous magnetization can be observed. The observed easy-plane ferromagnetic character agrees with the properties found in the bulk polycrystalline $Cr_{1/3}NbSe_2$ [28,29,37].

Due to the few-layer nature of the $Cr_{1/3}NbSe_2$ thin-film samples, it is nontrivial whether the band structure can be expected to exhibit a bulklike electronic structure predicted to host topological phases. To resolve this question, the overall three-dimensional (3D) electronic structure of the multilayer

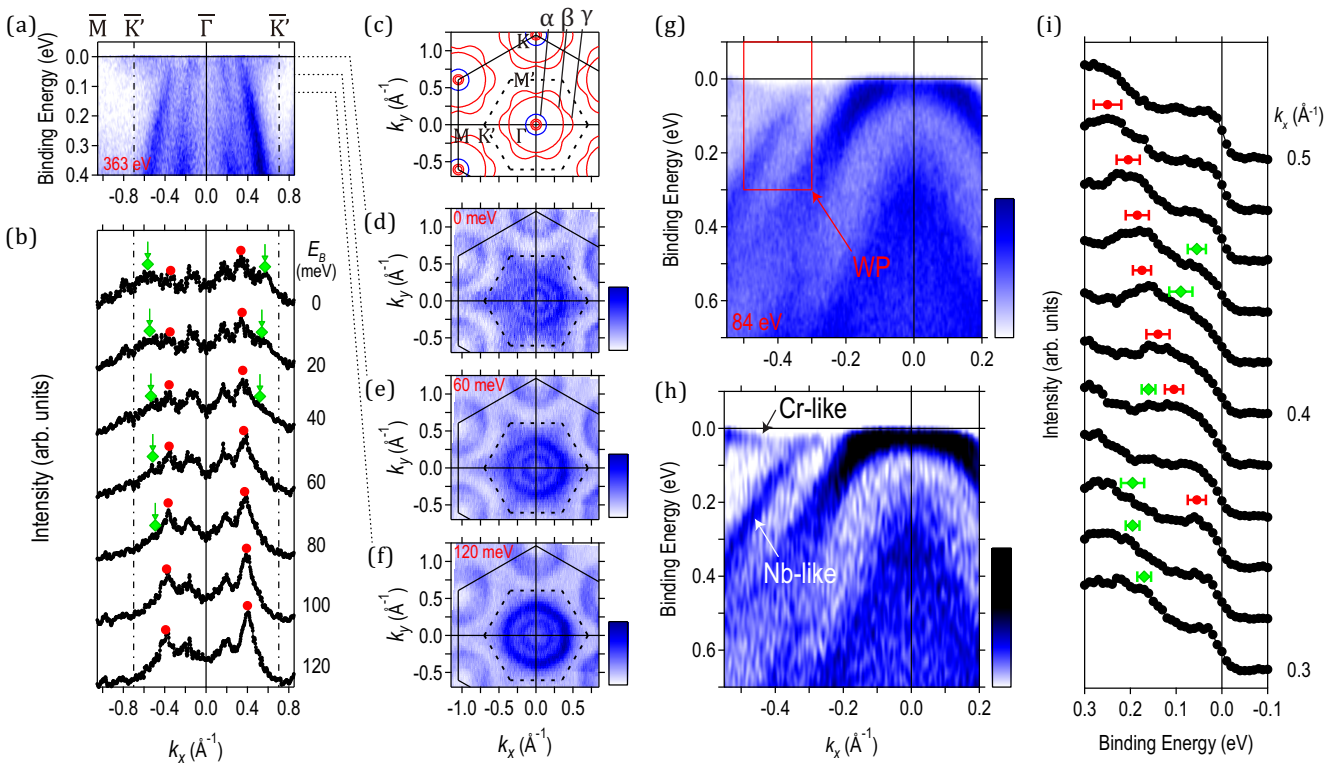

FIG. 4. Evidence of band crossing in the SX- and VUV-ARPES. (a) In-plane dispersion along $\overline{\Gamma}$-$\overline{M}$ taken with 363 eV photon energy. (b) Momentum distribution curves (integration width: 0.02 eV) along $\overline{\Gamma}$-$\overline{M}$. Green diamond (red circle) markers display bands with inward (outward) dispersion. (c) Calculated FS of $Cr_{1/3}NbSe_2$ showing corresponding α, β, and γ bands. (d)–(f) Constant energy maps taken at different binding energies showing the change to the "flowerlike" Fermi surface (integration width: 0.04 eV). (g) High-resolution VUV-ARPES measured with 84.5 eV photon energy along $\overline{\Gamma}$-$\overline{M}$. (h) Band filtering of the spectra in (g) using convolution of a 2D Gaussian filter. Arrows indicate bands participating in the crossing. (i) Energy distribution curves (integration width: 0.02 Å^{-1}). Peak plot traces Cr-like (green diamond) and Nb-like (red circle) bands.

$Cr_{1/3}NbSe_2$ was obtained via SX-ARPES, and the results are displayed in Fig. 3. The observed Fermi surface (FS) of $Cr_{1/3}NbSe_2$ is characterized mainly by the presence of two rather isotropic hole bands centered around $\overline{\Gamma}$ and $\overline{K}$, and one "flowerlike" shape around $\overline{\Gamma}$ as shown in Figs. 3(a) and 3(b). In Fig. 3(a), the smaller (larger) FS observed around $\overline{\Gamma}$ is labeled as the α band (β band), whereas the flowerlike FS is denoted as the γ band. The respective in-plane dispersion of the α and β bands together with the guide-for-the-eyes traces are displayed in Fig. 3(b). The Fermi momenta (k_F) along the $\overline{\Gamma}$-$\overline{M}$ direction (k_x) of the inner and outer bands were estimated to be roughly 0.16 and 0.34 Å^{-1}, respectively. We also display the band-unfolding calculation considering the ferromagnetic ground state without the inclusion of spin-orbit coupling (SOC) in Fig. 3(c). The minority- and majority-spin bands are depicted with blue and red markers, respectively. From the calculation results, it is possible to see the presence of two holelike bands with strong weight centered around Γ, respectively of spin down (inner) and spin up (outer), which agrees well with the measured α and β bands in Fig. 3(b). It is worth mentioning that such an agreement is lost when compared to the paramagnetic band structure displayed in Fig. 1(d), particularly regarding β bands which are absent in the corresponding energy momentum of the calculation.

ARPES experiments were further conducted by varying photon energies from 250 to 382 eV to characterize the electronic structure along the out-of-plane direction (k_z). The estimated value for the inner potential is 15.7 eV. Figure 3(d) schematically shows the measurement range. The FS measured along the k_x-k_z plane is displayed in Fig. 3(e), in which the solid red curve displays the k_z vs k_x cut taken with 363 eV shown in Figs. 3(a) and 3(b). Notably, α and β bands exhibit different degrees of dimensionality along k_z, namely α bands exhibit a 3D-like spheroidal FS, whereas β bands exhibit a cylindrical FS. The dispersion of the α bands along the k_z direction is shown in Fig. 3(f). The guide-for-the-eyes curve traces the main dispersive features of the α bands, showing strong three-dimensionality. The ARPES images without guide-for-the-eyes traces are given in the Supplemental Material [36]. Figure 3(g) shows the band-unfolding calculation results along the Γ-A direction. The presence of down-spin bands with strong k_z dispersion can be clearly visualized, being consistent with the previous claim regarding the correspondence between α (β) and down-spin bands (up-spin bands). This result suggests an electronic structure of multilayer $Cr_{1/3}NbSe_2$ close to the bulk. Indeed, the bulk band calculation is in good correspondence with ARPES, particularly when taking into account the 4π k_z periodicity of the

photoemission spectra. Considering the k_z dispersion, it is notable that the photoemission intensity of the α bands exhibits an apparent twofold period, repeating itself at every odd Γ point. Such a 4π period has been reported in other materials with a nonsymmorphic space group, such as T_d-$MoTe_2$ [38], T_d-WTe_2 [39], WSe_2 [40], and graphite [41]. Once such effects are taken into consideration, the agreement between the bulk and $Cr_{1/3}NbSe_2$ thin films' electronic structure becomes more apparent.

Now we examine the potential topological features of the bands obtained using SX- and VUV-ARPES. The low-energy features measured with 363 eV photons along k_x are displayed in Fig. 4(a). Although the previously mentioned β bands are strongly apparent, we can also discern the presence of additional intensity very close to E_F. By examining the momentum-distribution curves (MDCs), we can note the presence of an additional peak at roughly 0.57 Å^{-1} at $E_B = 0.0$ eV which shifts towards smaller momentum values at higher binding energies as shown by the green arrows in Fig. 4(b). The peaks eventually fade due to the strong intensity of the Nb-derived β bands burying the signal, indicating the crossing point around $E_B = 0.1$ eV. The feature resembles the dispersion of the γ bands described in Fig. 3(c). The calculated FS is shown in Fig. 4(c). The Cr-derived γ bands are observed to construct a "flowerlike" FS centered around Γ with the "petals" aligned along the Γ-M direction. To experimentally visualize the evolution of the γ band as it approaches the crossing point, the constant energy maps integrated over a 40 meV window are displayed in Figs. 4(d)–4(f). At the Fermi level [Fig. 4(d)], the flowerlike FS analogous to the calculation is clearly discernible, which shrinks with increasing E_B and eventually disappears at $E_B = 120$ meV.

Additional supporting evidence of the topological features was obtained via high-resolution VUV-ARPES measurements. Considering the photoionization of each element, the Cr $3d$ cross section relative to Nb $4d$ and Se $4p$ cross sections increases from the SX to VUV region [42]. The spectra measured along k_x with 84.5 eV photons are displayed in Fig. 4(g). To enhance the visibility of the band crossing, filtering of the ARPES image was performed by convolution of a two-dimensional (2D) Gaussian bandpass filter following the Fourier space approach in Fig. 4(h) [43]. Energy distribution curves (EDCs) also provide a visual guide to the observation of a weak but discernible signal of the band crossing in Fig. 4(i). Notably, both SX- and VUV-ARPES indicate the band crossing occurring at roughly $E_B = 0.1$ eV and momentum $k_x = 0.40$ Å^{-1}.

The topological nature of the observed band crossing can be understood from the twofold rotation symmetry (C_2) along the 100 axis in real space. This creates six Weyl nodes along Γ-M. The situation is analogous to the previously reported theoretical works on $V_{1/3}NbS_2$ and $Mn_{1/3}NbS_2$ [26]. In fact, the presence of the topological features is not restricted to the $Cr_{1/3}NbSe_2$ system, and similar Weyl nodes are expected to emerge with different intercalant atoms and host layers. Considering the wide variety of magnetic phases promoted by intercalation, $3d$ I-TMDCs provide the ideal platform to realize nontrivial topological systems with complex magnetic structures. Additionally, the layered nature of the $3d$ I-TMDCs provides further prospects towards different two-dimensional systems, as further tailoring of the magnetic and topological physics can be achieved in the three- to two-dimensional crossover. In this context, not only did we observe such topological features, but we also demonstrated its feasibility in epitaxial thin films fabricated via MBE. Such a thin-film approach to intercalated systems could readily expand the access to other magnetic Weyl semimetals, while providing routes towards functionalization in device applications. Prospects towards dimensionality control in magnetic systems as well as heterointerfaces could provide exciting and as yet unexplored perspectives in epitaxially grown $3d$ I-TMDCs.

In conclusion, by employing MBE, we successfully examined the electronic structure of epitaxially grown $Cr_{1/3}NbSe_2$. ARPES showed the three-dimensional character of the electronic structure, and a comparison with the bulk band calculation indicated the correspondence between the $Cr_{1/3}NbSe_2$ thin films and the bulk. We have identified the presence of a weak signal of the predicted band crossing, further evidencing $Cr_{1/3}NbSe_2$ as a potential ferromagnetic topological material. The present results provide proof-of-concept evidence of the MBE-grown $3d$-intercalated TMDCs as a platform towards different magnetic Weyl systems.

B.K.S. acknowledges the support by the World-leading Innovative Graduate Study Program for Materials Research, Information, and Technology (MERIT-WINGS) of the University of Tokyo. The measurements were performed under KEK-PF (Proposal No. 2020G634). This work was partly supported by the JSPS KAKENHI (No. JP19H05826, No. JP20H0183, No. JP21H05235, No. JP22H00107), CREST JST (No. JPMJCR20B4), and PRESTO JST (No. JPMJPR20L7).

[1] B. Keimer and J. E. Moore, The physics of quantum materials, Nat. Phys. **13**, 1045 (2017).

[2] Y. Tokura, M. Kawasaki, and N. Nagaosa, Emergent functions of quantum materials, Nat. Phys. **13**, 1056 (2017).

[3] D. N. Basov, R. D. Averitt, and D. Hsieh, Towards properties on demand in quantum materials, Nat. Mater. **16**, 1077 (2017).

[4] B. Yan and C. Felser, Topological materials: Weyl semimetals, Annu. Rev. Condens. Matter Phys. **8**, 337 (2017).

[5] A. Bernevig, H. Weng, Z. Fang, and X. Dai, Recent progress in the study of topological semimetals, J. Phys. Soc. Jpn. **87**, 041001 (2018).

[6] A. A. Burkov, Weyl metals, Annu. Rev. Condens. Matter Phys. **9**, 359 (2018).

[7] N. P. Armitage, E. J. Mele, and A. Vishwanath, Weyl and Dirac semimetals in three-dimensional solids, Rev. Mod. Phys. **90**, 015001 (2018).

[8] B. Q. Lv, H. M. Weng, B. B. Fu, X. P. Wang, H. Miao, J. Ma, P. Richard, X. C. Huang, L. X. Zhao, G. F. Chen,

Z. Fang, X. Dai, T. Qian, and H. Ding, Experimental Discovery of Weyl Semimetal TaAs, Phys. Rev. X **5**, 031013 (2015).

[9] L. X. Yang, Z. K. Liu, Y. Sun, H. Peng, H. F. Yang, T. Zhang, B. Zhou, Y. Zhang, Y. F. Guo, M. Rahn, D. Prabhakaran, Z. Hussain, S. K. Mo, C. Felser, B. Yan, and Y. L. Chen, Weyl semimetal phase in the non-centrosymmetric compound TaAs, Nat. Phys. **11**, 728 (2015).

[10] G. Bian, T. R. Chang, R. Sankar, S. Y. Xu, H. Zheng, T. Neupert, C. K. Chiu, S. M. Huang, G. Chang, I. Belopolski, D. S. Sanchez, M. Neupane, N. Alidoust, C. Liu, B. K. Wang, C. C. Lee, H. T. Jeng, C. Zhang, Z. Yuan, S. Jia *et al.*, Topological nodal-line fermions in spin-orbit metal $PbTaSe_2$, Nat. Commun. **7**, 10556 (2016).

[11] T. R. Chang, P. J. Chen, G. Bian, S. M. Huang, H. Zheng, T. Neupert, R. Sankar, S. Y. Xu, I. Belopolski, G. Chang, B. K. Wang, F. Chou, A. Bansil, H. T. Jeng, H. Lin, and M. Z. Hasan, Topological Dirac surface states and superconducting pairing correlations in $PbTaSe_2$, Phys. Rev. B **93**, 245130 (2016).

[12] K. Koepernik, D. Kasinathan, D. V. Efremov, S. Khim, S. Borisenko, B. Buchner, and J. van den Brink, $TaIrTe_4$: A ternary type-II Weyl semimetal, Phys. Rev. B **93**, 201101(R) (2016).

[13] E. Haubold, K. Koepernik, D. Efremov, S. Khim, A. Fedorov, Y. Kushnirenko, J. van den Brink, S. Wurmehl, B. Buchner, T. K. Kim, M. Hoesch, K. Sumida, K. Taguchi, T. Yoshikawa, A. Kimura, T. Okuda, and S. V. Borisenko, Experimental realization of type-II Weyl state in noncentrosymmetric $TaIrTe_4$, Phys. Rev. B **95**, 241108(R) (2017).

[14] M. Sakano, M. S. Bahramy, H. Tsuji, I. Araya, K. Ikeura, H. Sakai, S. Ishiwata, K. Yaji, K. Kuroda, A. Harasawa, S. Shin, and K. Ishizaka, Observation of spin-polarized bands and domain-dependent Fermi arcs in polar Weyl semimetal $MoTe_2$, Phys. Rev. B **95**, 121101(R) (2017).

[15] J. Jiang, Z. K. Liu, Y. Sun, H. F. Yang, C. R. Rajamathi, Y. P. Qi, L. X. Yang, C. Chen, H. Peng, C. C. Hwang, S. Z. Sun, S. K. Mo, I. Vobornik, J. Fujii, S. S. Parkin, C. Felser, B. H. Yan, and Y. L. Chen, Signature of type-II Weyl semimetal phase in $MoTe_2$, Nat. Commun. **8**, 13973 (2017).

[16] G. Chang, S. Y. Xu, X. Zhou, S. M. Huang, B. Singh, B. Wang, I. Belopolski, J. Yin, S. Zhang, A. Bansil, H. Lin, and M. Z. Hasan, Topological Hopf and Chain Link Semimetal States and Their Application to Co_2MnGa, Phys. Rev. Lett. **119**, 156401 (2017).

[17] I. Belopolski, K. Manna, D. S. Sanchez, G. Chang, B. Ernst, J. Yin, S. S. Zhang, T. Cochran, N. Shumiya, H. Zheng, B. Singh, G. Bian, D. Multer, M. Litskevich, X. Zhou, S. M. Huang, B. Wang, T. R. Chang, S. Y. Xu, A. Bansil *et al.*, Discovery of topological Weyl fermion lines and drumhead surface states in a room temperature magnet, Science **365**, 1278 (2019).

[18] D. F. Liu, A. J. Liang, E. K. Liu, Q. N. Xu, Y. W. Li, C. Chen, D. Pei, W. J. Shi, S. K. Mo, P. Dudin, T. Kim, C. Cacho, G. Li, Y. Sun, L. X. Yang, Z. K. Liu, S. S. Parkin, C. Felser, and Y. L. Chen, Magnetic Weyl semimetal phase in a kagomé crystal, Science **365**, 1282 (2019).

[19] Y. Okamura, S. Minami, Y. Kato, Y. Fujishiro, Y. Kaneko, J. Ikeda, J. Muramoto, R. Kaneko, K. Ueda, V. Kocsis, N. Kanazawa, Y. Taguchi, T. Koretsune, K. Fujiwara, A. Tsukazaki, R. Arita, Y. Tokura, and Y. Takahashi, Giant magneto-optical responses in magnetic Weyl semimetal $Co_3Sn_2S_2$, Nat. Commun. **11**, 4619 (2020).

[20] R. H. Friend, A. R. Beal, and A. D. Yoffe, Electrical and magnetic properties of some first row transition metal intercalates of niobium disulphide, Philos. Mag. **35**, 1269 (1977).

[21] S. S. P. Parkin and R. H. Friend, 3*d* transition-metal intercalates of the niobium and tantalum dichalcogenides. I. Magnetic properties, Philos. Mag. B **41**, 65 (1980).

[22] S. S. P. Parkin and R. H. Friend, 3*d* transition-metal intercalates of the niobium and tantalum dichalcogenides. II. Transport properties, Philos. Mag. B **41**, 95 (1980).

[23] N. J. Ghimire, A. S. Botana, J. S. Jiang, J. Zhang, Y. S. Chen, and J. F. Mitchell, Large anomalous Hall effect in the chiral-lattice antiferromagnet $CoNb_3S_6$, Nat. Commun. **9**, 3280 (2018).

[24] H. Tanaka, S. Okazaki, K. Kuroda, R. Noguchi, Y. Arai, S. Minami, S. Ideta, K. Tanaka, D. Lu, M. Hashimoto, V. Kandyba, M. Cattelan, A. Barinov, T. Muro, T. Sasagawa, and T. Kondo, Large anomalous Hall effect induced by weak ferromagnetism in the noncentrosymmetric antiferromagnet $CoNb_3S_6$, Phys. Rev. B **105**, L121102 (2022).

[25] X. P. Yang, H. LaBollita, Z.-J. Cheng, H. Bhandari, T. A. Cochran, J.-X. Yin, M. S. Hossain, I. Belopolski, Q. Zhang, Y. Jiang, N. Shumiya, D. Multer, M. Liskevich, D. A. Usanov, Y. Dang, V. N. Strocov, A. V. Davydov, N. J. Ghimire, A. S. Botana, and M. Z. Hasan, Visualizing the out-of-plane electronic dispersions in an intercalated transition metal dichalcogenide, Phys. Rev. B **105**, L121107 (2022).

[26] T. Inoshita, M. Hirayama, N. Hamada, H. Hosono, and S. Murakami, Topological semimetal phases manifested in transition metal dichalcogenides intercalated with 3*d* metals, Phys. Rev. B **100**, 121112(R) (2019).

[27] N. Sirica, S.-K. Mo, F. Bondino, I. Pis, S. Nappini, P. Vilmercati, J. Yi, Z. Gai, P. C. Snijders, P. K. Das, I. Vobornik, N. Ghimire, M. R. Koehler, L. Li, D. Sapkota, D. S. Parker, D. G. Mandrus, and N. Mannella, Electronic structure of the chiral helimagnet and 3*d*-intercalated transition metal dichalcogenide $Cr_{1/3}NbS_2$, Phys. Rev. B **94**, 075141 (2016).

[28] A. F. Gubkin, E. P. Proskurina, Y. Kousaka, E. M. Sherokalova, N. V. Selezneva, P. Miao, S. Lee, J. Zhang, Y. Ishikawa, S. Torii, T. Kamiyama, J. Campo, J. Akimitsu, and N. V. Baranov, Crystal and magnetic structures of $Cr_{1/3}NbSe_2$ from neutron diffraction, J. Appl. Phys. **119**, 013903 (2016).

[29] N. M. Toporova, E. M. Sherokalova, N. V. Selezneva, V. V. Ogloblichev, and N. V. Baranov, Crystal structure, properties and Griffiths-like phase in niobium diselenide intercalated with chromium, J. Alloys Compd. **848**, 156534 (2020).

[30] G. Kresse and J. Furthmuller, Efficient iterative schemes for *ab initio* total-energy calculations using a plane-wave basis set, Phys. Rev. B **54**, 11169 (1996).

[31] G. Kresse and J. Furthmüller, Efficiency of ab-initio total energy calculations for metals and semiconductors using a plane-wave basis set, Comput. Mater. Sci. **6**, 15 (1996).

[32] P. E. Blochl, Projector augmented-wave method, Phys. Rev. B **50**, 17953 (1994).

[33] G. Kresse and D. Joubert, From ultrasoft pseudopotentials to the projector augmented-wave method, Phys. Rev. B **59**, 1758 (1999).

[34] F. Hulliger and E. Pobitschka, On the magnetic behavior of new 2H-NbS_2-type derivatives, J. Solid State Chem. **1**, 117 (1970).

[35] B. V. Laar, H. M. Rietveld, and D. J. Ijdo, Magnetic and crystallographic structures of Me_xNbS_2 and Me_xTaS_2, J. Solid State Chem. **3**, 154 (1971).

[36] See Supplemental Material at http://link.aps.org/supplemental/10.1103/PhysRevResearch.4.L042021 for wide calculated band structure, XPS, ARPES image without guide-for-the-eyes and polarization dependence.

[37] W. Z. Hu, G. T. Wang, R. Hu, C. Petrovic, E. Morosan, R. J. Cava, Z. Fang, and N. L. Wang, Evidence for a band broadening across the ferromagnetic transition of $Cr_{1/3}NbSe_2$, Phys. Rev. B **78**, 085120 (2008).

[38] R. Ono, A. Marmodoro, J. Schusser, Y. Nakata, E. F. Schwier, J. Braun, H. Ebert, J. Minár, K. Sakamoto, and P. Krüger, Surface band characters of the Weyl semimetal candidate material $MoTe_2$ revealed by one-step angle-resolved photoemission theory, Phys. Rev. B **103**, 125139 (2021).

[39] D. Di Sante, P. K. Das, C. Bigi, Z. Ergönenc, N. Gürtler, J. A. Krieger, T. Schmitt, M. N. Ali, G. Rossi, R. Thomale, C. Franchini, S. Picozzi, J. Fujii, V. N. Strocov, G. Sangiovanni, I. Vobornik, R. J. Cava, and G. Panaccione, Three-Dimensional Electronic Structure of the Type-II Weyl Semimetal WTe_2, Phys. Rev. Lett. **119**, 026403 (2017).

[40] T. Finteis, M. Hengsberger, T. Straub, K. Fauth, R. Claessen, P. Auer, P. Steiner, S. Hüfner, P. Blaha, M. Vögt, M. Lux-Steiner, and E. Bucher, Occupied and unoccupied electronic band structure of WSe_2, Phys. Rev. B **55**, 10400 (1997).

[41] F. Matsui, H. Nishikawa, H. Daimon, M. Muntwiler, M. Takizawa, H. Namba, and T. Greber, The $4\pi k_z$ periodicity in photoemission from graphite, Phys. Rev. B **97**, 045430 (2018).

[42] J. J. Yeh and I. Lindau, Atomic subshell photoionization cross sections and asymmetry parameters: $1 \leqslant z \leqslant 103$, At. Data Nucl. Data Tables **32**, 1 (1985).

[43] R. Li, X. Zhang, L. Miao, L. Stewart, E. Kotta, D. Qian, K. Kaznatcheev, J. T. Sadowski, E. Vescovo, A. Alharbi, T. Wu, T. Taniguchi, K. Watanabe, D. Shahrjerdi, and L. A. Wray, Second derivative analysis and alternative data filters for multi-dimensional spectroscopies: A Fourier-space perspective, J. Electron Spectrosc. Relat. Phenom. **238**, 146852 (2020).